Optical and Quantum Electronics (2026) 58:359
https://doi.org/10.1007/s11082-026-08964-4

# $ScBr_2$/AlSe: a magnetic dihalide/non-magnetic chalcogenide van der Waals heterostructure from first principles

**Neslihan Gokcek[1] · Aysenur Gencer[2] · Gokhan Surucu[3] · Ozge Surucu[4,5]**

Received: 19 April 2026 / Accepted: 9 June 2026
© The Author(s) 2026

**Abstract**
Combining intrinsic 2D ferromagnetism with a broadband optoelectronic response within a single van der Waals (vdW) architecture remains an open design challenge. Here, first-principles density-functional-theory calculations are used to investigate the $ScBr_2$/AlSe vdW heterostructure, representing the first coupling of a magnetic transition-metal dihalide with a non-magnetic group-III chalcogenide. The low lattice mismatch ($\delta \approx 2.17\%$) yields three energetically near-degenerate stacking configurations within PBE+D3 accuracy; the heteroB stacking is adopted as the representative geometry and its dynamical, thermal and mechanical stability is confirmed through phonon dispersion, machine-learned-force-field-accelerated ab-initio molecular dynamics at 300 K, and Born-stable elastic constants. HSE06 calculations yield a direct gap of 0.57 eV with clear Type-II band-edge character, and the $ScBr_2$ magnetic moment is preserved at 1.0 μB per Sc atom. The optical response shows strong absorption across the visible and ultraviolet regions with in-plane isotropy. These results establish the transition-metal-dihalide/group-III-chalcogenide class as a promising design space for multifunctional magnetic–optoelectronic vdW heterostructures.

**Keywords** Density functional theory · Van der Waals heterostructure · 2D ferromagnetic semiconductor · Type-II band alignment · Machine-learned force field · Scandium dihalide

✉ Ozge Surucu
ozgesurucu@aybu.edu.tr

[1] Electrical and Electronics Engineering Department, Atilim University, 06836 Ankara , Turkey

[2] Department of Physics, K. O. Faculty of Science, Karamanoglu Mehmetbey University, 70200 Karaman, Turkey

[3] Department of Energy Systems Engineering, Faculty of Technology, Gazi University, 06500 Ankara, Turkey

[4] Department of Energy Systems Engineering Faculty of Engineering and Natural Sciences, Ankara Yildirim Beyazıt University, 06010 Ankara, Turkey

[5] The Center for Third Generation Solar Cells Research and Applications (SOLAR 3.0), Ankara Yıldırım Beyazıt University, Ankara, Turkey

Published online: 17 June 2026

## 1 Introduction

Since the isolation of graphene (Novoselov et al. 2016), the two-dimensional (2D) materials library has grown to encompass transition-metal dichalcogenides, black phosphorus, hexagonal boron nitride, group-III chalcogenides, MXenes and transition-metal halides, each contributing distinct electronic, optical or magnetic functionalities to the flatland platform (Chaves et al. 2020). A common limitation, however, is that no single monolayer simultaneously offers ferromagnetic order, a broad optical response in the visible range, and mechanical compliance for strain engineering. The construction of vertical van der Waals (vdW) heterostructures, in which two dissimilar monolayers are stacked to produce a composite electronic structure distinct from either constituent, has emerged as an effective strategy for combining complementary properties within a single atomically thin architecture (Oh et al. 2024).

Among the band-edge alignments that arise upon stacking, the staggered Type-II configuration is particularly attractive for 2D optoelectronics. Its spatial separation of photogenerated electrons and holes on opposite sides of the interface suppresses radiative recombination and prolongs carrier lifetimes, directly enhancing photocatalytic and photovoltaic performance (Rawat et al. 2019; Singh et al. 2024). Recent first-principles studies have reported theoretical solar-to-hydrogen efficiencies above 20% in GaSe/BiSCl, and $Ga_2SSe/SnSSe$ Type-II heterobilayers (Xiao et al. 2026, Yang et al. 2025). Complementary to the built-in band offset, mechanical strain provides a continuous degree of freedom for tuning the fundamental gap and toggling between direct and indirect transitions (Boland et al. 2024). Most of these Type-II systems, however, pair two closed-shell semiconductors, so the spin degree of freedom plays no active role at the interface. Incorporating magnetism into a Type-II vdW heterostructure would add spin polarization on top of the existing charge-separation mechanism, combining optoelectronic and spintronic functionalities within a single interface.

The 2D magnetic-materials field has matured rapidly since the experimental confirmation of intrinsic ferromagnetism in monolayer $CrI_3$ and $Cr_2Ge_2Te_6$ (Zhang et al. 2024; Jia et al. 2025), with most efforts concentrated on Cr- and Fe-based systems paired with TMD or graphene partners (Pan et al. 2024). The scandium dihalide $ScX_2$ (X = Cl, Br, I) family offers an alternative starting point: these monolayers have been predicted to be in-plane ferromagnetic semiconductors with preserved out-of-plane symmetry, a $d^1$ Sc configuration that localizes the conduction-band minimum in Sc-d states, and a mechanically compliant 1 T framework (Wu et al. 2023; Chen et al. 2020). On the non-magnetic side, the group-III aluminum monochalcogenides AlX (X = O, S, Se, Te) are well-established 2D semiconductors with HSE06 gaps spanning the visible range, band edges that straddle the water redox potentials, and confirmed dynamical and thermal stabilities (Haman et al. 2021, Chen et al. 2019). AlSe in particular combines a buckled Se–Al–Al–Se motif with robust mechanical stiffness and has recently been incorporated into strain-engineered SiTe/AlSe heterostructures for hydrogen evolution and broadband optoelectronics (Talib et al. 2026). Bringing these two families together within a single coherent vdW interface has, to the best of our knowledge, not yet been reported from first principles.

Motivated by this, the present work presents a first-principles density-functional-theory investigation of a magnetic-transition-metal-dihalide/non-magnetic-group-III-chalcogenide vdW heterostructure, realized in the $ScBr_2$/AlSe combination. $ScBr_2$ was selected for its

favourable lattice match with AlSe ($\delta \approx 2.17\%$), which keeps the interface coherent and minimizes strain-induced defect formation. Three stacking configurations are fully relaxed and their energetic, dynamical, thermal (via machine-learned-force-field-accelerated ab-initio molecular dynamics) and mechanical stabilities are verified. The electronic structure is characterized at both the PBE and HSE06 levels, including orbital-resolved band edges and the spin-polarized density of states, while the optical response is analyzed through the complex dielectric function, absorption, reflectivity and transmission, with explicit attention to the limits of the independent-particle approximation. The resulting picture identifies the $ScBr_2$/AlSe heterostructure as a mechanically compliant, magnetically ordered, broadband-absorbing 2D system with Type-II band-edge character, providing a concrete example of how the transition-metal-dihalide/group-III-chalcogenide class can yield multifunctional magnetic-optoelectronic vdW architectures.

## 2 Calculation details

In this study, $ScBr_2$ and AlSe monolayers, in addition to the heterostructures formed by these monolayers, were investigated using the density functional theory (DFT) based Vienna Ab-initio Simulation Package (VASP) (Kresse and Furthmüller 1996, Kresse and Furthmüller 1996). The Perdew-Burke-Ernzerhof (PBE) functional (Perdew et al. 1996) was utilized within the Generalized Gradient Approximation (GGA) to calculate the exchange-correlation terms in electron-electron interactions. The Projector Augmented Wave (PAW) method (Kresse and Joubert 1999, Blöchl 1994) was employed to account for electron-ion interactions in the calculations. The monolayers and heterostructures were fully relaxed with a plane-wave cut-off energy of 520 eV. Convergence thresholds for the total energy and Hellmann–Feynman forces were set to $10^{-6}$ eV and $10^{-3}$ eV/Å, respectively. The **k**-points were sampled using a gamma centered scheme (Pack and Monkhorst 1977) with $15 \times 15 \times 1$ **k**-points for the monolayers and $9 \times 9 \times 1$ **k**-points for the heterostructures. A vacuum region of at least 15 Å along the z-direction was introduced to suppress spurious interactions between periodic images. The valence electron configurations adopted in the PAW potentials were $3d^14s^2$, $4s^24p^5$, $3s^23p^1$, and $4s^24p^4$ for Sc, Br, Al and Se, respectively. Van der Waals interactions were incorporated via Grimme's DFT-D3 dispersion correction with zero-damping (Grimme et al. 2010). The mechanical stability of these monolayers was examined by determining the elastic constants using the energy-strain method, implemented in the ELASTOOL program (Kastuar et al. 2022, Liu et al. 2022). The dynamical stabilities of these monolayers were determined by means of phonon dispersion curves, which are obtained using the Phonopy program (Togo 2023, Witman et al. 2023). The Phonopy program employs the finite displacement method for these calculations. The electronic band gaps were first obtained at the PBE level. Because PBE is known to underestimate semiconductor band gaps, the screened Heyd–Scuseria–Ernzerhof hybrid functional (HSE06) (Heyd et al. 2003) was used to obtain more accurate band gaps, with a screening parameter of 0.2 $Å^{-1}$ (Krukau et al. 2006). Furthermore, the exchange element is mixed with 25% of the exact non-local Hartree-Fock exchange (Krukau et al. 2006). Band structures were plotted using the Sumo toolkit (Ganose et al. 2018). Furthermore, the ab-initio molecular dynamics calculations were obtained using a $2 \times 2 \times 1$ supercell at the ambient pressure and 300 K temperature. The atomic positions and the lattice parameters were used as the dynamical

variables. In this study, the Langevin thermostat (Evans 1983, Lemons and Gythiel 1908) was utilized with 10 $ps^{-1}$, 12 $ps^{-1}$, 7 $ps^{-1}$, 12 $ps^{-1}$, and 9 $ps^{-1}$ atomic frictions for the Sc, Br, Al, Se atoms and lattice frictions, respectively, in order to achieve the desired results. The Verlet algorithm was applied to integrate the equations of motion related to the ions with an integration time step of 2 fs. For the AIMD calculations, the k-points were taken as $5 \times 5 \times 1$. As is well documented, AIMD calculations are computationally expensive and time-consuming. This encourages the implementation of machine-learned force fields in VASP (Jinnouchi et al. 2020, Jinnouchi et al. 2019). In the context of machine-learned potential energy surfaces, the descriptors based on the Gaussian representation of atomic distributions (Jinnouchi et al. 2020, Behler and Parrinello 2007) have been demonstrated to offer a robust and effective framework for description and analysis. Moreover, the target properties, encompassing energy, forces, and stress tensor components, were obtained through Bayesian linear regression (Jinnouchi et al. 2019, Bishop 2006), a process that yields reliable estimates. Crystal visualizations were acquired through the utilization of a software program known as VESTA (Momma and Izumi 2011).

## 3 Results and discussions

### 3.1 Structural optimizations of $ScBr_2$ and AlSe monolayers and their heterostructure

The optimized crystal structures of the $ScBr_2$ and AlSe monolayers are illustrated in Fig. 1, which displays the top and side views of their respective $2 \times 2 \times 1$ supercells to visualize the lattice and atomic arrangements more explicitly. $ScBr_2$ crystallizes in a trigonal symmetry where the Sc atom is octahedrally coordinated by six Br atoms, whereas AlSe exhibits a hexagonal lattice characterized by a buckled Se–Al–Al–Se sequence. As listed in Table 1, the calculated lattice parameters (a) for $ScBr_2$ and AlSe are 3.68 Å and 3.76 Å , respectively, which are consistent with the available literature for these monolayers. The calculated bond lengths, measured at 2.75 Å for Sc–Br and 2.46 Å/2.57 Å for Al–Se and Al–Al, further dem-

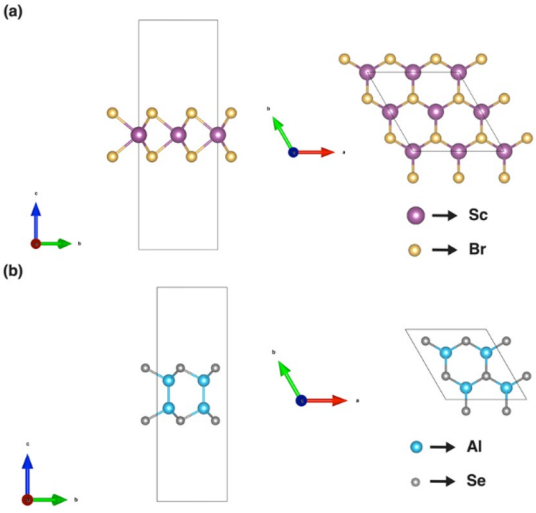



**Fig. 1** Side and top view of the crystal structures of the $2 \times 2 \times 1$ supercells of the **a** $ScBr_2$ and **b** AlSe monolayers

**Table 1** The lattice parameter (a in Å), bond lengths ($d_{X-Y}$ in Å), cohesive energy ($E_{coh}$ in eV/atom), for the $ScBr_2$ and AlSe monolayers

| Monolayer | a | $d_{X-Y}$ | $E_{coh}$ |
|---|---|---|---|
| $ScBr_2$ | 3.68 | 2.75 (Sc–Br) | −1.67 |
| | 3.721 (Wu et al. 2023) | | |
| | 3.758 (Chen et al. 2020) | | |
| AlSe | 3.76 | 2.46 (Al–Se)/2.57 (Al–Al) | −0.85 |
| | 3.776 (Haman et al. 2021) | 2.472 (Al–Se)/2.586 (Al–Al) (Haman et al. 2021) | |
| | 3.70 (Chen et al. 2019) | 2.45 (Al–Se)/2.57 (Al–Al) (Chen et al. 2019) | |

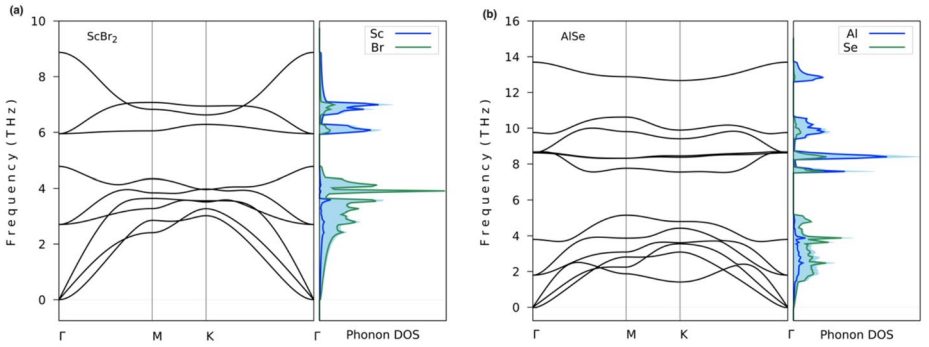



**Fig. 2** Phonon dispersion curves for **a** $ScBr_2$ and **b** AlSe monolayers

onstrate the reliability of the PBE+D3 functional in describing these systems. The cohesive energy ($E_{coh}$) per atom was evaluated following the definition of (Mehta et al. 2024) and the obtained results are listed in Table 1 which are negative indicating the energetic stability and therefore the potential synthesizability of these monolayers; the larger magnitude obtained for $ScBr_2$ indicates a more robust crystal framework than that of AlSe.

Furthermore, the formation of the heterostructure is governed by the lattice mismatch $\delta$, which was determined to be approximately 2.17% based on the optimized monolayer parameters. This low mismatch value is well within the acceptable threshold for van der Waals heterojunctions, suggesting that a coherent interface can be maintained with minimal strain-induced defects. This structural compatibility implies that the $ScBr_2$ layer will be subjected to a slight tensile strain while the AlSe layer undergoes compressive strain in the combined system, providing a potential mechanism for tuning the electronic properties of the heterojunction.

In addition to the energetic stability, the dynamical stability of the $ScBr_2$ and AlSe monolayers was rigorously examined through their phonon dispersion curves using $4 \times 4 \times 1$ supercell with 0.01 Å displacement amplitude, as illustrated in Fig. 2. For both systems, the absence of imaginary frequency modes throughout the entire Brillouin zone confirms that these monolayers are dynamically stable and correspond to true local minima on the potential energy surface. This stability is consistent with the negative cohesive energies reported in Table 1, which were calculated following the methodology described in (Mehta et al. 2024) and indicate robust energetic favorability for both structures.

In the right panels of Fig. 2a and b, the calculated phonon density of states (Phonon DOS) provides further insight into the vibrational characteristics of the lattices. A clear mass-dependent distribution is observed; the heavier Br and Se atoms contribute more significantly to the lower frequency branches due to their higher atomic masses compared to the Sc and Al atoms. Notably, the optical branches in AlSe reach frequencies as high as approximately 14 THz, whereas those in $ScBr_2$ extend only to ~9 THz. This discrepancy suggests that the Al–Se and Al–Al covalent bonds are significantly stiffer than the Sc–Br bonds, reflecting the stronger interatomic interactions in the AlSe monolayer.

A critical observation in the $ScBr_2$ spectrum is the presence of a phonon band gap between 5 THz and 6 THz, which is absent in the AlSe monolayer. This gap has profound implications for the thermal and electronic properties of the resulting heterojunction. From a thermal perspective, the mismatch in phonon spectra and the existence of this gap can increase interfacial thermal resistance by limiting the transmission of vibrational modes between the two layers. Electronically, the phonon gap may reduce electron-phonon scattering rates for high-energy carriers, potentially leading to enhanced carrier mobility within the $ScBr_2$ layer of the heterostructure.

Furthermore, the ZA (out-of-plane) acoustic modes in both monolayers exhibit the characteristic quadratic dispersion near the $\Gamma$ point, which is a hallmark of flexible 2D membranes. This mechanical flexibility, combined with the frequency-filtering nature of the phonon gap, suggests that the $ScBr_2$/AlSe heterojunction is an excellent candidate for straintronics and thermal management applications, where external strain can be used to precisely tune both the electronic band gaps and the heat dissipation characteristics.

To investigate the structural stability and determine the preferred atomic registry, three distinct stacking configurations—denoted as heteroA, heteroB, and heteroC—were constructed using $2 \times 2 \times 1$ supercells of the $ScBr_2$ and AlSe monolayers, as illustrated in Fig. 3. Each configuration was fully optimized, and their respective binding energies ($E_{bind}$) were calculated following the methodology described in (Nasoz et al. 2025). The optimized structural parameters, including the lattice constant (a), interlayer distance (d), and binding energies, are summarized in Table 2. The results indicate that all three stacking modes converge to an identical lattice parameter of 7.45 Å, reflecting a balanced strain distribution between the constituent layers. The three configurations are energetically near-degenerate, with binding-energy differences of only 0.7–1.8 meV/atom, i.e. within the intrinsic accuracy of PBE+D3. Among them, heteroB exhibits the marginally lowest binding energy (−0.6736 eV/atom) and was therefore adopted as the representative stacking for all subsequent electronic, mechanical and optical calculations. Interestingly, heteroB also displays the largest interlayer distance of 3.32 Å. After determining the most stable stacking, the ferromagnetic and antiferromagnetic configurations were considered in order to determine the most stable magnetic configuration and as can be seen from Figure S1, the ferromagnetic configuration is the most stable. Therefore, the following discussions were obtained using the ferromagnetic configuration of the heteroB structure.

To efficiently sample the potential energy surface while preserving first-principles accuracy, the interatomic forces driving the AIMD trajectory were described by machine-learned force fields (MLFF). The reliability of this approach is confirmed in Fig. 4, which presents the Bayesian error and the root-mean-square error (RMSE) of forces for the heteroB configuration over a 10 ps trajectory.

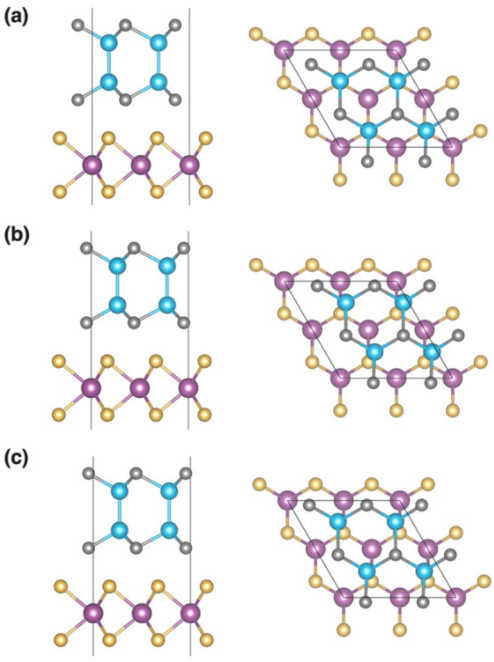



**Fig. 3** Crystal structures of $ScBr_2$/AlSe heterostructures for **a** heteroA, **b** heteroB, and **c** heteroC stackings

**Table 2** The lattice parameter (a in Å), binding energy ($E_{bind}$ in eV/atom), and the distance between the monolayers (d in Å) for the heteroA, heteroB, and heteroC

| Heterostructure | a | $E_{bind}$ | d |
|---|---|---|---|
| HeteroA | 7.45 | −0.6729 | 3.28 |
| HeteroB | 7.45 | −0.6736 | 3.32 |
| HeteroC | 7.45 | −0.6718 | 3.27 |

As illustrated in Fig. 4a, the Bayesian error of the forces remains consistently low, generally fluctuating below 0.020 eV/Å throughout the 10,000 fs simulation. This indicates that the MLFF model was effectively trained and did not encounter atomic configurations significantly outside its known local environments, ensuring high confidence in the predicted ionic trajectories. Furthermore, as shown in Fig. 4b, the RMSE of the forces maintains an exceptionally small magnitude, in the order of $10^{-4}$ eV/Å. These low error metrics demonstrate that the MLFF-driven AIMD provides a highly accurate description of the interatomic forces, comparable to direct DFT methods but with significantly enhanced computational efficiency.

The preservation of the structural integrity throughout the 10 ps simulation at ambient temperature, supported by these low error values, confirms that the $ScBr_2$/AlSe heterojunction is thermally stable and suitable for practical device applications. The stability of the Bayesian error suggests that the 10 ps timescale was sufficient to sample the local potential energy surface without the system drifting into unstable or disordered phases. Additionally, the exceptionally low RMSE value (approximately $1.12 \times 10^{-4}$ eV/Å) indicates that the MLFF successfully captured the subtle van der Waals interactions at the interface. These

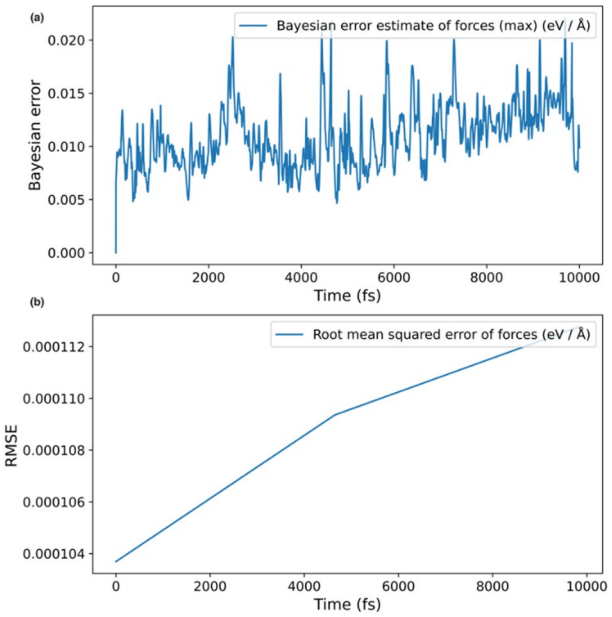



**Fig. 4** **a** the Bayesian error of the MLFF and **b** the root-mean-square error (RMSE) of forces for the heteroB

MD results complement the phonon dispersion findings, providing a complete picture of stability ranging from the T = 0 K dynamical limit to finite-temperature thermal fluctuations.

The thermodynamic stability of the heteroB configuration was rigorously evaluated through ab-initio molecular dynamics (AIMD) simulations at a constant temperature of 300 K. Figure 5a and b illustrate the evolution of the total energy and temperature, respectively, over a 10,000 fs (10 ps) trajectory. As shown in Fig. 5a, the total energy of the system remains remarkably stable, fluctuating around a mean value of approximately − 128.0 eV with no discernible downward or upward drift. Simultaneously, Fig. 5b demonstrates that the temperature fluctuations, controlled by the Langevin thermostat, consistently oscillate around the target value of 300 K. These minimal fluctuations indicate that the $ScBr_2$/AlSe heterostructure exists in a deep, stable potential well, confirming its structural integrity at ambient conditions.

Furthermore, the initial and final crystal structures are displayed as insets in Fig. 5. A comparison between these snapshots reveals no significant bond breaking, atomic layer distortion, or layer separation, suggesting a high mechanical stiffness that resists thermal degradation. The preservation of the atomic registry and the van der Waals gap throughout the simulation time substantiates that the heteroB stacking is not only the ground-state configuration at 0 K but is also thermally robust. Specifically, the interatomic distances in the final snapshot remain within the range of the optimized values, confirming that the tensile and compressive strains required to match the lattices did not introduce structural weaknesses. These findings, supported by the low machine-learning force field (MLFF) errors and the consistent behavior of the trajectory, provide strong evidence that the $ScBr_2$/AlSe heterojunction is suitable for practical experimental synthesis and device operation at room temperature.

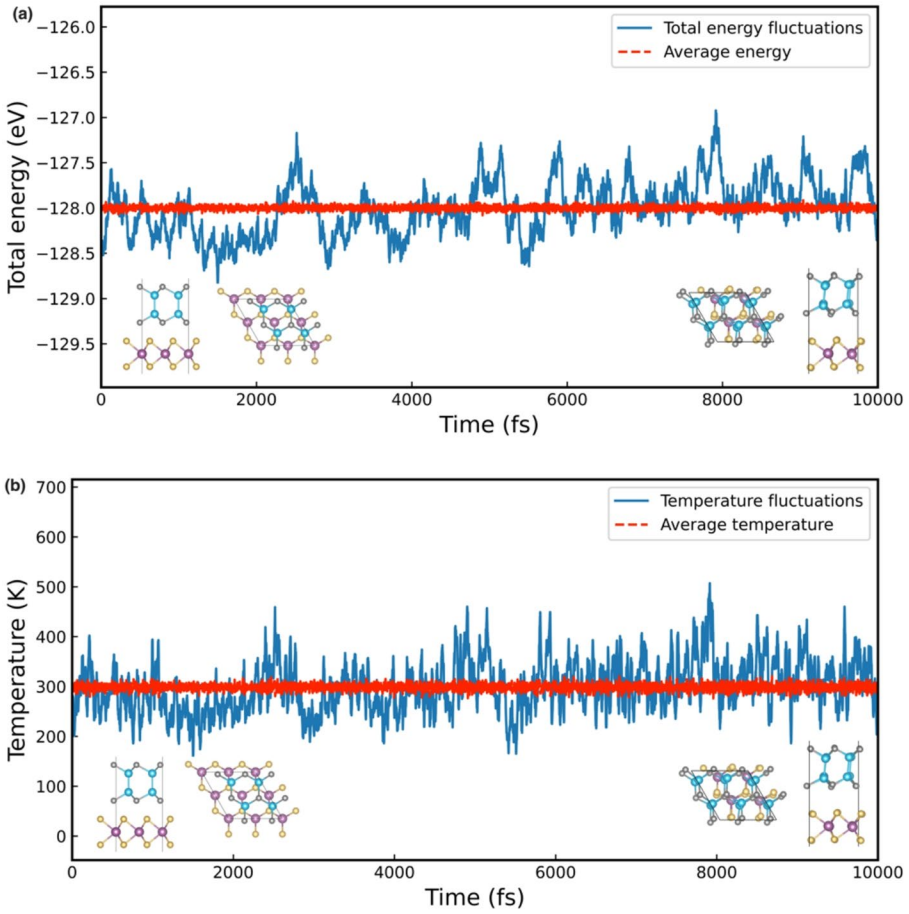



**Fig. 5** **a** Total energy and **b** temperature variation over 10,000 fs during AIMD calculations for the heteroB

**Table 3** The elastic constants ($C_{11}$ and $C_{12}$ in N/m), Young's modulus ($Y_{2D}$ in N/m), shear modulus ($G_{2D}$ in N/m), and Poisson's ratio ($\nu$) for the $ScBr_2$ and AlSe monolayers and their heterostructure

| Monolayer | $C_{11}$ | $C_{12}$ | $Y_{2D}$ | $G_{2D}$ | $\nu$ |
|---|---|---|---|---|---|
| $ScBr_2$ | 53.13 | 16.69 | 47.88 | 18.22 | 0.31 |
| AlSe | 73.69 | 18.50 | 69.04 | 27.59 | 0.25 |
| HeteroB | 124.97 | 33.97 | 115.74 | 45.50 | 0.27 |

## 3.2 Mechanical properties of $ScBr_2$ and AlSe monolayers and their heterostructure

Having established the energetic stability of the monolayers and their heterostructure, we next computed the elastic constants using the energy–strain method implemented in the ELASTOOL program; the results are listed in Table 3. Figure 6 displays the alteration in strain energy density as a function of strain for the $ScBr_2$ and AlSe monolayers and their heterostructure. As is evident in the figure, higher strain energy densities are obtained for the 0.03, −0.03 and ± 0.03 strains for $ScBr_2$, AlSe and their heterostructure, respectively. The

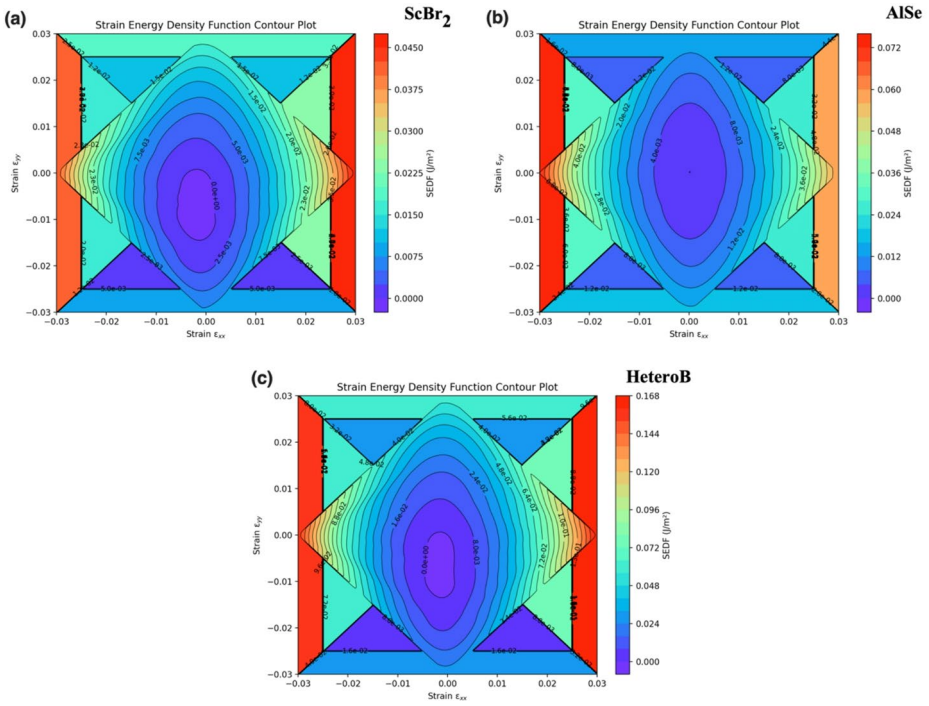



**Fig. 6** Strain energy density change as a function of strain for the **a** $ScBr_2$, **b** AlSe, and **c** heteroB

continuous and positive quadratic nature of the strain energy density surface for all three systems confirms that they reside in a stable mechanical equilibrium. Moreover, the heterostructure attains a maximum value of about $0.168\,\mathrm{J/m^2}$, indicating that it exhibits greater resistance to mechanical deformation compared to the isolated monolayers.

These monolayers have a hexagonal structure, and the necessary elastic constants are $C_{11}$ and $C_{12}$ for any 2D hexagonal structure (Wang et al. 2022). As demonstrated in Table 3, the elastic constants of both the $ScBr_2$ and AlSe monolayers, as well as their heterostructure, strictly comply with these rules, thereby ensuring their mechanical stability. Also, for a 2D structure to be mechanically stable, the Born stability rules (Wang et al. 2022, Born and Huang 1954) must be met. For hexagonal structures, this means $C_{11}$ must be more than zero and $C_{11}$ must be more than the absolute value of $C_{12}$. As demonstrated in Table 3, the elastic constants of these monolayers comply with the Born stability rules, thereby ensuring mechanical stability. The Young's modulus ($Y_{2D}$), shear modulus ($G_{2D}$), and Poisson's ratio (v) for these monolayers are also listed in Table 3. The $Y_{2D}$ is the in-plane rigidity of the 2D materials and, as the table shows, the heteroB has the highest value among these materials. This ensures that the mechanical performance of the heterojunction will be uniform regardless of the direction of the applied in-plane load. The relatively low Young's modulus of these materials (compared to graphene's ~ 340 N/m (Lee et al. 1979) suggests they are quite flexible. This flexibility, combined with the quadratic ZA modes observed in the phonon spectra, confirms that the $ScBr_2$/AlSe heterojunction is an ideal candidate for straintronics, where small mechanical deformations can be used to tune the electronic band gap. The $G_{2D}$

is the material's reaction to shear stress, and it is vital for the 2D materials due to determining the material's conduct under in-plane shear loads. The $G_{2D}$'s behavior is similar to the $Y_{2D}$'s of these materials. The parameter known as the Poisson ratio is defined by the ratio of the transverse strain to the longitudinal strain, thereby reflecting the response to uniaxial strain. As Table 3 shows, the $ScBr_2$ has the highest ν value among these materials indicating a higher degree of transverse contraction when stretched longitudinally. To further elucidate the mechanical nature of these systems, the polar plots for ν and $Y_{2D}$ are displayed in Fig. 7. As this figure shows, these monolayers have an anisotropic character in ν and $Y_{2D}$ along the

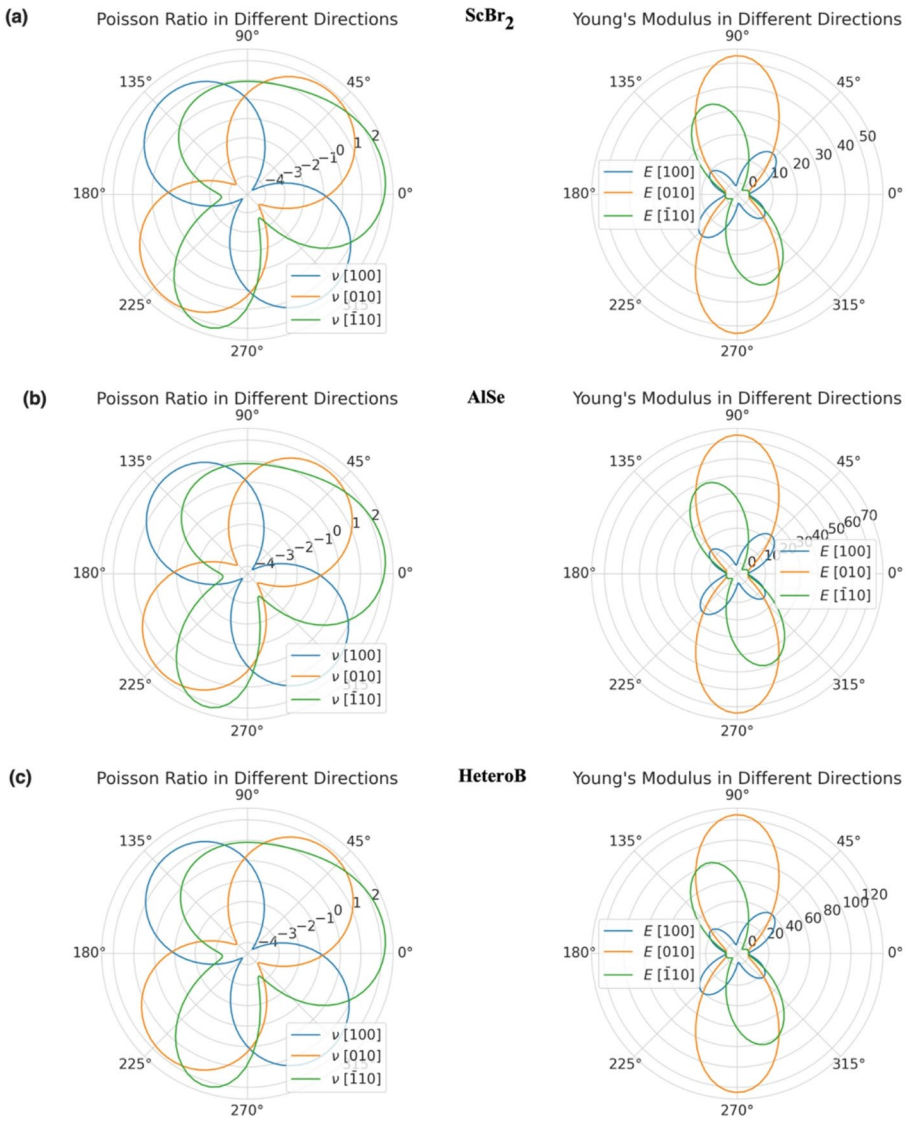



**Fig. 7** Polar plots for the Poisson's ratio and Young's modulus for the **a** $ScBr_2$, **b** AlSe, and **c** heteroB along the different lattice planes

different lattice planes. The directional dependence of $Y_{2D}$ reveals that the in-plane rigidity is not uniform, with the maximum stiffness consistently aligned along specific crystallographic axes. The similarity in the "shape" of the polar plots across all three figures confirms that the 2.17% lattice mismatch does not significantly distort the mechanical symmetry of the layers when they are combined into a heterojunction. The high anisotropy in $Y_{2D}$ suggests that the electronic properties (band gap tuning) will also be highly dependent on the direction of the applied strain. This anisotropic mechanical profile is a critical finding for the design of nanodevices such as directional sensors or actuators, as it allows for the optimization of device performance by aligning the strain-sensitive components along the most rigid or compliant directions of the heterostructure.

### 3.3 Electronic properties of $ScBr_2$ and AlSe monolayers and their heterostructure

The electronic band structures of the $ScBr_2$, AlSe and their heterostructure were obtained using the PBE and HSE methods. The PBE method is known to underestimate the band gap of the semiconductors, so the HSE06 method is used to obtain band gaps that are consistent with the experimental ones. Figure 8 shows the band structures that were obtained using the PBE method,

where the indirect band gaps of the $ScBr_2$, AlSe and their heterostructure are 0.12 eV, 1.87 eV and 0.10 eV, respectively. For the $ScBr_2$ monolayer and the heterostructure, the magnetic moments were considered and the band structures were visualized both for spin-up and spin-down states. Furthermore, the magnetic moments were determined as 1.0 $\mu_B$ and 4.0 $\mu_B$ for the $ScBr_2$ and the heterostructure, respectively. In addition, the corresponding density of states (DOS) for these materials are shown in Fig. 8 in the right panels. For the $ScBr_2$ monolayer, the most contributions come from d states of Sc atoms and p states of Br atoms above and below the Fermi level, respectively. For the AlSe monolayer, the most contributions come from the p states of Se atom both above and below the Fermi level. For the heterostructure, the most contributions come from the d states of Sc and p states of Se

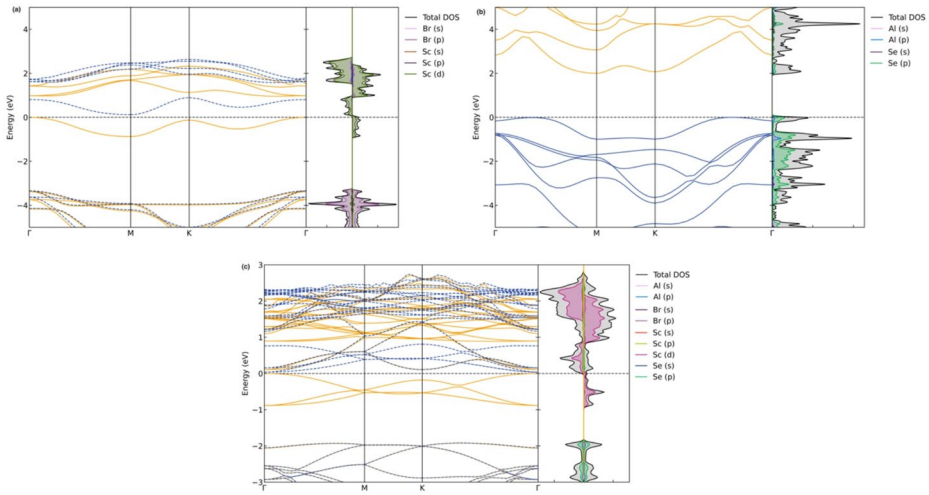



**Fig. 8** The electronic band structures for the **a** $ScBr_2$, **b** AlSe, and **c** their heterostructure obtained using the PBE method

above and below the Fermi level, respectively and the system maintains an indirect bandgap, slightly reduced to 0.10 eV under the PBE functional. The total magnetic moment of the heterostructure cell is 4.0 $\mu_B$ which corresponds to exactly 1.0 μB per Sc atom (four Sc atoms in the $2 \times 2 \times 1$ supercell), identical to the per-atom moment of the isolated $ScBr_2$ monolayer. This indicates that the Sc local moment is preserved upon heterostructure formation rather than genuinely enhanced by interlayer coupling; the total value of 4.0 μB therefore reflects supercell scaling rather than a cooperative magnetic effect. Furthermore, the persistence of distinct spin-splitting in the heterostructure makes it a promising candidate for spintronic applications, where the spin degree of freedom can be utilized for advanced information processing. The asymmetry between spin-up and spin-down states near the Fermi level in the heterostructure implies its potential use in spin-filtering devices, where only one spin component is allowed to transport. The DOS for the heterostructure reveals that the valence band maximum (VBM) is now primarily derived from Se p states of the AlSe layer, while the (conduction band) CBM remains dominated by the Sc-d states of the $ScBr_2$ layer. This spatial separation of charge carriers between the layers indicates a spontaneous interlayer charge transfer at the interface. This orbital decomposition is consistent with a Type-II band-edge character, which, if corroborated by plane-averaged electrostatic potential analysis with vacuum-level-aligned band edges and a quantitative Bader-based interlayer charge-transfer analysis, would be highly desirable for optoelectronic and photovoltaic applications such as solar cells and photodetectors, as it facilitates efficient electron–hole separation. Additionally, the small PBE band gap of 0.10 eV for the heterostructure suggests the system is near a metal-semiconductor transition, which could potentially be triggered by an out-of-plane electric field or external strain.

Figure 9 illustrates the electronic band structures for these monolayers obtained using the HSE06 method. The indirect band gaps of the $ScBr_2$, AlSe and direct band gap of the heterostructure have been found to be 0.17 eV, 2.56 eV and 0.57 eV, respectively. The band gap of the $ScBr_2$ monolayer is reported as 0.148 eV obtained using the PBE method in (Chen et al. 2020) and 0.55 eV obtained using the DFT+U method in (Wu et al. 2023). The band gap of the AlSe monolayer is reported as 2.012 eV and 2.740 eV obtained using the PBE and HSE06 methods in (Haman et al. 2021) and 2.01 eV obtained using the PBE method in (Chen et al. 2019). Therefore, the results of this study are consistent with those in the literature. A critical finding in Fig. 9c is the transition of the heterostructure from an indirect bandgap (under PBE) to a direct bandgap of 0.57 eV under the HSE06 functional. This direct transition at the Γ point is highly advantageous for optoelectronic applications, as it significantly enhances the light absorption and emission efficiency. The HSE06

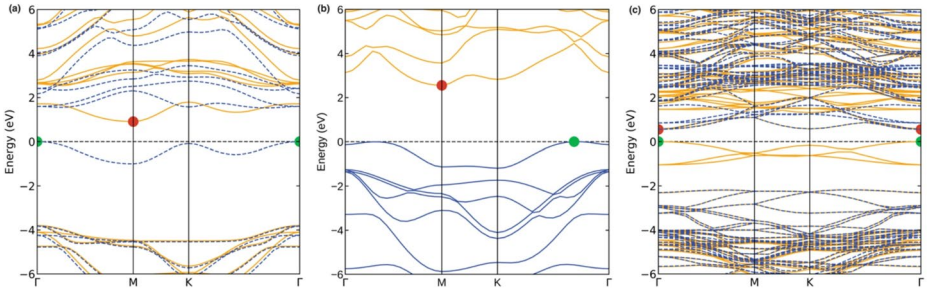



**Fig. 9** The electronic band structures for the **a** $ScBr_2$, **b** AlSe, and **c** their heterostructure obtained using the HSE method

results confirm the persistence of strong spin-polarization in the $ScBr_2$-based systems. The increased gap separation between spin-up and spin-down states compared to PBE suggests that $ScBr_2$ maintains a robust ferromagnetic ground state, making it a viable candidate for high-temperature flexible spintronics. The curvature of the bands at the CBM and VBM in the HSE06 plots remains relatively sharp, suggesting that the effective masses of charge carriers are low. This implies that the $ScBr_2$/AlSe heterostructure likely possesses high carrier mobility, similar to other aluminum chalcogenides reported in the literature. Furthermore, the Curie temperature is important for the magnetic materials and it was determined for the heteroB using the mean-field approximation $k_B T_C = {}^2/_3 \, \Delta E$ (Pan et al. 2017) where $k_B$ is the Boltzmann constant and $\Delta E$ is the energy difference between the ferromagnetic and antiferromagnetic configurations. The calculated Curie temperature is 206 K which implies robust magnetism around the room temperature and as a result, the heteroB is a suitable candidate for the spintronics applications.

### 3.4 Optical properties of $ScBr_2$ and AlSe monolayers and their heterostructure

In addition to the electronic structure, the optical response of these systems was investigated through the frequency-dependent complex dielectric function defined in Eq. (1) (Mehta et al. 2023).

$$\varepsilon(\omega) = \varepsilon_1(\omega) + i\varepsilon_2(\omega) \tag{1}$$

In Eq. (1), $\varepsilon_1(\omega)$ is the real and $\varepsilon_2(\omega)$ is the imaginary part of the dielectric function. This function can be used to obtain the absorption (A). It can also be used to obtain the reflection (R) and the transmission (T). Since the monolayers are 2D materials, the parameters are given in normalized values because of the slab thickness. Please note that the sum of the A+R + T must be equal to 1. Figures 10a, 11a, and 12a demonstrate the real and imaginary part of the dielectric function across the xx and yy directions for the $ScBr_2$, AlSe, and heterostructure, correspondingly. The real part of the dielectric function has been found to have 4.14, 3.71, and 4.86 values at 0 eV for the $ScBr_2$, AlSe, and heterostructure, respectively. This enhancement in the heterostructure suggests stronger polarizability due to interlayer

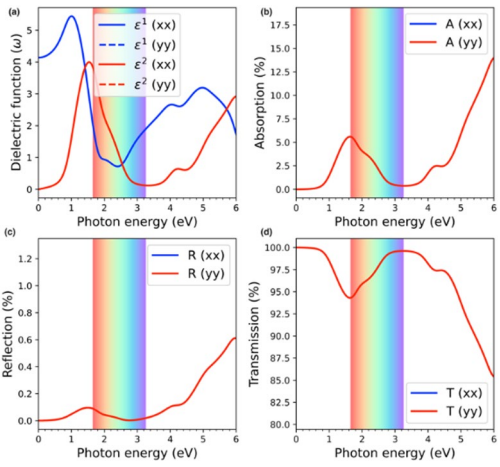



**Fig. 10** **a** Real and imaginary parts of the dielectric function, **b** absorption, **c** reflection, and **d** transmission spectra of the $ScBr_2$ monolayer (the visible light region is marked with a rainbow bar)

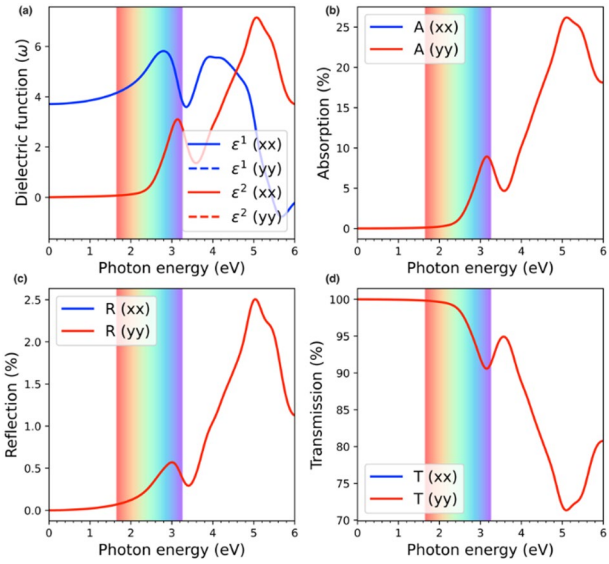



**Fig. 11** **a** Real and imaginary parts of the dielectric function, **b** absorption, **c** reflection, and **d** transmission spectra of the AlSe monolayer (the visible light region is marked with a rainbow bar)

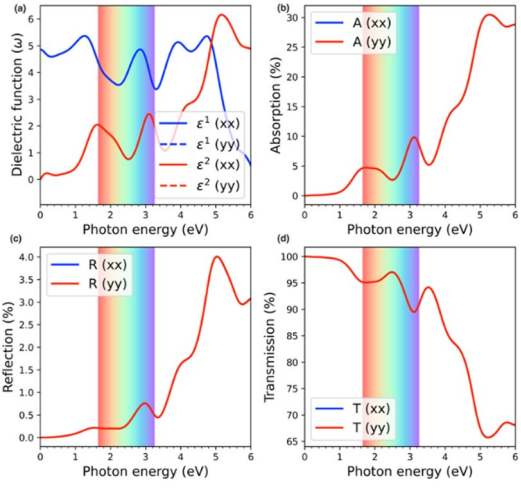



**Fig. 12** **a** Real and imaginary parts of the dielectric function, **b** absorption, **c** reflection, and **d** transmission spectra of the heterostructure (the visible light region is marked with a rainbow bar)

coupling and charge redistribution at the interface. When the spectrum of the real part of the dielectric function is analyzed, there are no negative values, indicating the semiconducting character of these monolayers between 0 and 6 eV (Barma et al. 2023). Furthermore, the nearly identical curves for the xx and yy directions indicate that these materials exhibit in-plane optical isotropy, which is advantageous for device fabrication as it ensures uniform performance regardless of the orientation of in-plane polarized light.

The imaginary component of the dielectric function is also displayed in the figures pertaining to the optical band gaps. As the figures show, the optical band gaps of the ScBr$_2$, AlSe, and heterostructure are 0.10 eV, 1.92 eV, and 0.13 eV, respectively. The electronic band gaps obtained using the GGA-PBE method have been shown to be consistent with these results. It should be emphasized, however, that these optical spectra are computed

within the independent-particle approximation on top of the PBE electronic structure, and therefore inherit the well-known PBE underestimation of the fundamental gap. The physically meaningful absorption onset of the heterostructure is consequently expected to shift from 0.13 eV to a value close to the HSE06 fundamental gap (0.57 eV), placing the true onset in the near-infrared rather than the deep-infrared regime. This caveat should be kept in mind throughout the following discussion of absorption, reflection and transmission spectra. Within this caveat, the HSE06-corrected absorption onset of the heterostructure falls in the near-infrared (≈2.18 μm at 0.57 eV), positioning the system as a near-infrared-to-visible broadband absorber rather than a deep-infrared detector. In Fig. 12a, the heterostructure shows a unique $\epsilon_2$ peak structure that is not a simple superposition of the constituent monolayers. This non-trivial feature indicates interlayer orbital hybridization and a redistribution of single-particle oscillator strengths upon heterostructure formation. It should be emphasized, however, that the present optical properties are computed within the independent-particle approximation (IPA) via the LOPTICS tag in VASP on top of the PBE electronic structure. The major limitation of the IPA framework is that it completely neglects many-body electron-hole interactions (excitonic effects), which are exceptionally strong in 2D monolayers and heterostructures due to reduced dimensional dielectric screening. Quantitatively accounting for these effects requires a highly demanding Bethe–Salpeter-equation (BSE) calculation on top of a G0W0 quasiparticle band structure, which remains beyond the computational scope of this study. Qualitatively, the inclusion of excitonic effects via BSE would introduce two primary changes to the optical spectra: first, a notable redistribution of oscillator strength into sharp, bound excitonic peaks accompanied by a significant spectral redshift governed by the excitonic binding energy (Eb). Second, owing to the Type-II band alignment of the ScBr2/AlSe interface, the formation of spatially separated interlayer excitons would occur. These interlayer excitons would manifest as low-energy bound states below the fundamental gap edge, offering prolonged carrier lifetimes beneficial for photovoltaic extraction. This many-body context should be kept in mind when interpreting the independent-particle absorption profiles presented herein. The higher $\varepsilon_1(0)$ of the heterostructure (4.86) compared to the monolayers indicates reduced Coulombic interaction between carriers. This high dielectric screening is beneficial for photovoltaic applications, as it facilitates the dissociation of excitons into free charge carriers, thereby potentially increasing the quantum efficiency of the device. The primary peaks of $\varepsilon_2$ for the heterostructure occur around 1.6 eV and 3.1 eV. This indicates that while the material has an IR onset, its maximum energy dissipation and strongest light-matter interaction occur in the visible and near-UV regions, providing a broad spectral coverage.

Figures 10b, 11b, and 12b illustrate the absorption along the xx and yy directions for the $ScBr_2$, AlSe, and heterostructure, respectively. All three systems exhibit strong absorption that extends from the visible into the ultraviolet, with the principal absorption peaks located in the UV region. Furthermore, Fig. 13 shows the absorption spectrum for $ScBr_2$, AlSe and heterostructure in the same plot in order to compare easily. As can be seen from this figure, the heterostructure has higher absorption in the visible ranger than $ScBr_2$ and AlSe monolayers. A primary finding is the significant redshift in the absorption onset of the heterostructure compared to the AlSe monolayer. While the AlSe monolayer is largely transparent to infrared (IR) radiation with an onset near 2.0 eV, the heterostructure initiates absorption at approximately 0.13 eV. This shift extends the operational range into the IR regime, rendering it superior to the SiTe/AlSe system, which maintains a much larger

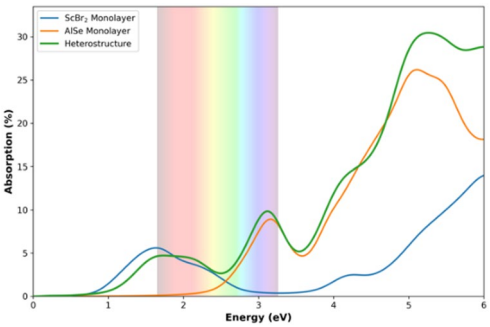



**Fig. 13** Absorption spectrum for ScBr$_2$, AlSe, and their heterostructure

indirect gap of 2.30 eV and is less efficient for IR detection (Talib et al. 2026). Compared to benchmark transition metal dichalcogenide (TMD) systems such as $MoS_2/WS_2$ (Nguyen et al. 2025), which often show limited absorption efficiency or sharp declines in the UV-C range (approximately 4.4–6.2 eV), heteroB maintains high and rising absorption levels up to 6 eV. This sustained activity across the high-energy range, together with the strong visible-region response, indicates broadband optoelectronic utility spanning the visible and ultraviolet regions. We note that "solar-blind" operation (i.e. selective sensitivity to deep-UV with suppressed visible response) is not applicable to the present system, since its narrow fundamental gap (0.57 eV at HSE06) inherently produces strong interband absorption throughout the visible range. The identical absorption profiles for xx and yy polarizations confirm that the material's light-harvesting efficiency is independent of the polarization angle of incident light. This simplifies the design of photovoltaic cells, as it eliminates the need for specific crystal orientation to maximize solar capture. The combination of high absorption in the visible/UV range and the Type-II band alignment (which facilitates carrier separation) marks the ScBr2/AlSe system as a highly efficient candidate for the next generation of thin-film solar cells. The exceptionally low lattice mismatch of 2.17% ensures that the absorption properties are not degraded by strain-induced defects, a common issue in high-performance systems like $GaSe/MoS_2$ (Pham et al. 2018) where higher mismatch often compromises optical quality. Unlike non-magnetic benchmarks like GaSe/InSe (Novoselov et al. 2016), the ScBr2/AlSe system combines broadband absorption (from IR to UV) with intrinsic ferromagnetism carried by the Sc sublattice (1.0 $\mu_B$ per Sc atom).

Figures 10c, 11c, and 12c demonstrate the reflection along the xx and yy directions for the ScBr$_2$, AlSe, and heterostructure, respectively. The reflectivity vanishes at zero photon energy, increases monotonically with photon energy, and reaches its maximum in the UV region. The nearly identical curves for the xx and yy directions confirm the in-plane optical isotropy of these structures, a critical factor for designing omnidirectional optical coatings and sensors where surface reflection losses must remain independent of the polarization angle. When compared to benchmark 2D van der Waals (vdW) systems, the ScBr2/AlSe heterostructure demonstrates superior characteristics, such as minimized visible reflection losses (below 1.0% in the 1.6–3.1 eV range), which significantly outperforms transition metal dichalcogenides (TMDs) like $MoS_2$ (Gerbi 2025) that often exceed 5–10% reflectivity due to excitonic effects. Furthermore, the heterostructure exhibits a sharp rising trend in UV-C reflectance towards 4.0% at 5.0 eV, offering more effective high-energy filtering than the flat profiles of h-BN (Harikrishnan et al. 2024). The reflectivity peak near 3.0 eV in the heterostructure is notably higher than that of the isolated AlSe monolayer, reflecting

an enhanced surface polarizability induced by the Type-II band alignment and interlayer charge redistribution. This synergistic interface effect, coupled with an exceptionally low lattice mismatch of 2.17%, ensures high-fidelity optical performance devoid of the scattering noise seen in highly strained heterostructures like $CrI_3$/graphene (Tseng et al. 2022). Consequently, the low reflectivity ($R < 1\%$ across the 1.6–3.1 eV window) is consistent with useful antireflective behavior at the front interface of photovoltaic absorber stacks. We emphasize, however, that the small fundamental gap (0.57 eV at HSE06) precludes visible-transparent conducting-electrode applications: strong interband absorption across the entire visible range renders the heterostructure optically opaque, so it cannot serve the same role as wide-gap transparent conductors such as ITO, graphene or h-BN.

Figures 10d, 11d, and 12d illustrate the transmission along the xx and yy directions for the $ScBr_2$, AlSe, and heterostructure, respectively. The transmission is high at low photon energies and decreases monotonically as the photon energy increases, in accordance with the complementary behavior of the absorption spectra ($A + R + T = 1$). We emphasize that the apparent high visible transmission of the PBE-based spectrum is an artefact of the PBE underestimation of the fundamental gap; within the HSE06 gap of 0.57 eV, strong interband absorption is expected across the visible range, rendering the heterostructure optically opaque in the visible regime. The sharp decline in transmission above 4.0 eV (falling toward 65% at 6.0 eV) is more pronounced than in wider-bandgap systems like h-BN or SiTe/AlSe, establishing the heterostructure as an effective natural UV-C filter. Additionally, the exceptionally low lattice mismatch of 2.17% minimizes interface scattering centers, leading to smoother transmission curves and fewer extrinsic losses compared to high-mismatch systems like GaSe/$MoS_2$. The combination of a direct 0.57 eV gap, strong absorption across the visible-to-UV range, and intrinsic magnetic ordering positions this heterostructure as a candidate absorber layer for thin-film photovoltaic and spintronic device architectures, rather than as a transparent window layer.

## 4 Conclusion

This work has presented a comprehensive first-principles density-functional-theory investigation of the $ScBr_2$/AlSe van der Waals heterostructure and its constituent monolayers, representing the first systematic study of a magnetic-transition-metal-dihalide/non-magnetic-group-III-chalcogenide 2D interface. The small lattice mismatch of 2.17% allows the two monolayers to form a coherent heterojunction in which three stacking configurations (heteroA, heteroB, heteroC) emerge as energetically near-degenerate minima within the intrinsic accuracy of the PBE+D3 functional. The heteroB stacking, with an interlayer separation of 3.32 Å, was adopted as the representative geometry for all subsequent electronic, mechanical and optical analyses. Its energetic, dynamical, thermal and mechanical stabilities were confirmed through cohesive and binding energies, phonon dispersion curves devoid of imaginary frequencies, machine-learned-force-field-accelerated ab-initio molecular dynamics at 300 K over a 10 ps trajectory, and elastic constants satisfying the Born stability criteria.

The electronic structure obtained with the HSE06 hybrid functional shows that $ScBr_2$/AlSe is a direct-gap semiconductor with a fundamental gap of 0.57 eV at the Γ point, accompanied by a clear Type-II band-edge character: the valence-band maximum is derived

from Se-p states of the AlSe layer, while the conduction-band minimum retains Sc-d character from the $ScBr_2$ layer. The magnetic moment of the $ScBr_2$ sublattice is preserved upon heterostructure formation at 1.0 μB per Sc atom, and the spin polarization persists in the combined system, offering a native spintronic degree of freedom that is absent in conventional chalcogenide-only Type-II heterostructures. The 2D Young's modulus of 115.7 N/m, essentially additive from the constituent monolayer values, confirms the weak interlayer coupling characteristic of a vdW system while preserving each layer's intrinsic in-plane stiffness. The optical response, evaluated within the independent-particle approximation, reveals strong absorption from the visible into the ultraviolet region with in-plane optical isotropy; we emphasize that the true absorption onset is expected to follow the HSE06 fundamental gap of 0.57 eV rather than the PBE-derived 0.13 eV, a caveat important for any quantitative device-level projection.

Beyond the specific $ScBr_2$/AlSe system, these results establish the transition-metal-dihalide/group-III-chalcogenide family as an underexplored but physically well-motivated design space for 2D heterostructures in which intrinsic ferromagnetism, broadband optical absorption and mechanical compliance are co-hosted within a single coherent vdW interface.

**Supplementary Information** The online version contains supplementary material available at https://doi.org/10.1007/s11082-026-08964-4.

**Acknowledgements** As detailed in this study, the numerical calculations were performed using TRUBA resources at TUBITAK ULAKBIM, High Performance and Grid Computing Centre, and at Istanbul Technical University National Center for High-Performance Computing. This latter institution, which is known as ITU-UHEM, has a grant number for this project of 1024042025.

**Author contributions** N.G. and A.G. performed the first-principles calculations and analyzed the electronic and structural properties of the monolayers. A.G., G.S and O.S. investigated the optical and mechanical properties, including the implementation of the machine-learned force field accelerated AIMD simulations. N.G, A.G and O.S. wrote the main manuscript text. N.G. and A.G. prepared the figures and tables, including crystal visualizations and polar plots. All authors reviewed and approved the final version of the manuscript.

**Funding** Open access funding provided by the Scientific and Technological Research Council of Türkiye (TÜBİTAK).

**Data availability** The datasets generated and analyzed during the current study are available from the corresponding author on reasonable request. The computational data (VASP input/output files and MLFF results) supporting the findings of this research are stored in the authors' institutional repository and can be provided for validation purposes.

## Declarations

**Competing interests** The authors declare no competing interests.

**Open Access** This article is licensed under a Creative Commons Attribution 4.0 International License, which permits use, sharing, adaptation, distribution and reproduction in any medium or format, as long as you give appropriate credit to the original author(s) and the source, provide a link to the Creative Commons licence, and indicate if changes were made. The images or other third party material in this article are included in the article's Creative Commons licence, unless indicated otherwise in a credit line to the material. If material is not included in the article's Creative Commons licence and your intended use is not permitted by statutory regulation or exceeds the permitted use, you will need to obtain permission directly from the copyright holder. To view a copy of this licence, visit http://creativecommons.org/licenses/by/4.0/.

## References


Barma, S., Hasan Khan, M.S., Islam, M.R., Hasan, M.T.: Intralayer spatial carrier separation capability for visible light driven photocatalytic properties of SnGe2N4-layered nanostructure: A first-principles study. AIP Adv. **13**, 75020 (2023). https://doi.org/10.1063/5.0160594/2902238

Behler, J., Parrinello, M.: Generalized Neural-Network Representation of High-Dimensional Potential-Energy Surfaces. Phys. Rev. Lett. **98**, 146401 (2007). https://doi.org/10.1103/PhysRevLett.98.146401

Bishop, C.M.: Pattern Recognition and Machine Learning. (2006)

Blöchl, P.E.: Projector augmented-wave method. Phys. Rev. B **50**, 17953 (1994). https://doi.org/10.1103/PhysRevB.50.17953

Boland, C.S., Sun, Y., Papageorgiou, D.G.: Bandgap engineering of 2D Materials toward high-performing straintronics. Nano Lett. (2024). https://doi.org/10.1021/acs.nanolett.4c03321

Born, M., Huang, K.: Dynamical theory of crystal lattices. Oxford University Press (1954)

Chaves, A., Azadani, J.G., Alsalman, H., da Costa, D.R., Frisenda, R., Chaves, A.J., et al.: Bandgap engineering of two-dimensional semiconductor materials. NPJ 2D Mater. Appl. **4**, 29 (2020). https://doi.org/10.1038/s41699-020-00162-4

Chen, W., Chen, X., Wu, Y., Liu, G., Pan, H.: First-principles investigation of $ScX_2$ (X=Cl, Br, or I) monolayers for flexible spintronic and electronic applications. Phys. Chem. Chem. Phys. **22**, 14781–14786 (2020). https://doi.org/10.1039/D0CP02222E

Chen, X., Huang, Y., Liu, J., Yuan, H., Chen, H.: Thermoelectric performance of two-dimensional AlX (X=S, Se, Te): a first-principles-based transport study. ACS Omega **4**, 17773–81 (2019). https://doi.org/10.1021/acsomega.9b02235

Evans, D.J.: Computer 'experiment' for nonlinear thermodynamics of Couette flow. J. Chem. Phys. **78**, 3297–3302 (1983). https://doi.org/10.1063/1.445195

Ganose, A.M., Jackson, A.J., Scanlon, D.O.: sumo: Command-line tools for plotting and analysis of periodic *ab initio* calculations. J. Open. Source Softw. **3**, 717 (2018). https://doi.org/10.21105/JOSS.00717

Gerbi, Z.D.: Electronic and optical properties of molybdenum disulfide (MoS2) mono layer using density functional theory (DFT) calculations. AIP Adv. (2025). https://doi.org/10.1063/5.0256769

Grimme, S., Antony, J., Ehrlich, S., Krieg, H.: A consistent and accurate ab initio parametrization of density functional dispersion correction (DFT-D) for the 94 elements H-Pu. J. Chem. Phys. (2010). https://doi.org/10.1063/1.3382344/926936

Haman, Z., Khossossi, N., Kibbou, M., Bouziani, I., Singh, D., Essaoudi, I., et al.: Computational identification of efficient 2D Aluminium chalcogenides monolayers for optoelectronics and photocatalysts applications. Appl. Surf. Sci. **556**, 149561 (2021). https://doi.org/10.1016/j.apsusc.2021.149561

Harikrishnan, K., Hoque, A., Patel, R., Singh, V.P., Gaur, U.K., Sharma, M.: Electronic, electrical, and optical properties of hexagonal boron nitride. In: Hexagonal Boron Nitride, pp. 89–123. Elsevier (2024). https://doi.org/10.1016/B978-0-443-18843-5.00019-7

Heyd, J., Scuseria, G.E., Ernzerhof, M.: Hybrid functionals based on a screened Coulomb potential. J. Chem. Phys. **118**, 8207–8215 (2003). https://doi.org/10.1063/1.1564060

Jia, Z., Zhao, M., Chen, Q., Tian, Y., Liu, L., Zhang, F., et al.: Spintronic devices upon 2D magnetic materials and heterojunctions. ACS Nano. **19**, 9452–83 (2025). https://doi.org/10.1021/acsnano.4c14168

Jinnouchi, R., Karsai, F., Verdi, C., Asahi, R., Kresse, G.: Descriptors representing two-and three-body atomic distributions and their effects on the accuracy of machine-learned inter-atomic potentials. J. Chem. Phys. (2020). https://doi.org/10.1063/5.0009491/946337

Jinnouchi, R., Karsai, F., Kresse, G.: On-the-fly machine learning force field generation: Application to melting points. Phys. Rev. B. **100**, 014105 (2019). https://doi.org/10.1103/PhysRevB.100.014105

Kastuar, S.M., Ekuma, C.E., Liu, Z.L.: Efficient prediction of temperature-dependent elastic and mechanical properties of 2D materials. Sci. Rep. **12**, 1 (2022). https://doi.org/10.1038/s41598-022-07819-8

Kresse, G., Furthmüller, J.: Efficient iterative schemes for ab initio total-energy calculations using a plane-wave basis set. Phys. Rev. B **54**, 11169 (1996). https://doi.org/10.1103/PhysRevB.54.11169

Kresse, G., Furthmüller, J.: Efficiency of ab-initio total energy calculations for metals and semiconductors using a plane-wave basis set. Comput. Mater. Sci. **6**, 15–50 (1996). https://doi.org/10.1016/0927-0256(96)00008-0

Kresse, G., Joubert, D.: From ultrasoft pseudopotentials to the projector augmented-wave method. Phys. Rev. B **59**, 1758 (1999). https://doi.org/10.1103/PhysRevB.59.1758

Krukau, A.V., Vydrov, O.A., Izmaylov, A.F., Scuseria, G.E.: Influence of the exchange screening parameter on the performance of screened hybrid functionals. J. Chem. Phys. (2006). https://doi.org/10.1063/1.2404663/953719

Lemons, D.S., Gythiel, A.: Paul Langevin's 1908 paper On the Theory of Brownian Motion [Sur la théorie du mouvement brownien, C. R. Acad. Sci. (Paris) 146, 530–533 ]. Am J Phys 1997;65:1079–81. (1908). https://doi.org/10.1119/1.18725

Lee, C., Wei, X., Kysar, J.W., Hone, J.: Measurement of the Elastic Properties and Intrinsic Strength of Monolayer Graphene. Science **321**, 385–8 (1979). https://doi.org/10.1126/science.1157996

Liu, Z.L., Ekuma, C.E., Li, W.Q., Yang, J.Q., Li, X.J.: ElasTool: an automated toolkit for elastic constants calculation. Comput. Phys. Commun. **270**, 108180 (2022). https://doi.org/10.1016/J.CPC.2021.108180

Mehta, D., Naik, Y., Modi, N., Parmar, P.R., Thakor, P.B.: A computational study on strain dependent photocatalytic activity of Janus Ga-Al-X-Se (X = S and Se) monolayers. Comput. Mater. Sci. **236**, 112861 (2024). https://doi.org/10.1016/J.COMMATSCI.2024.112861

Mehta, D., Naik, Y., Modi, N., Parmar, P.R., Thakor, P.B.: A theoretical investigation on optoelectronic and photocatalytic behaviour of Janus X-Ga-Al-Y (X, YS and Te) monolayers. Solid State Commun. **375**, 115347 (2023). https://doi.org/10.1016/J.SSC.2023.115347

Momma, K., Izumi, F.: VESTA 3 for three-dimensional visualization of crystal, volumetric and morphology data. Urn:Issn:0021-8898. **44**, 1272–1276 (2011). https://doi.org/10.1107/S0021889811038970

Nasoz, D.L., Surucu, O., Wang, X., Surucu, G., Sarac, Y., Gencer, A.: Penta-Graphene/SnS2Heterostructures with Z-scheme Charge Transfer for Efficient Photocatalytic Water Splitting. J. Phys. Chem. C. **129**, 16767–16779 (2025). https://doi.org/10.1021/ACS.JPCC.5C03664/. (**SUPPL_FILE/JP5C03664_SI_001.PDF**)

Nguyen, H.T., Le, V.L., Nguyen, T.M., Bui, X.K., Nguyen, T.G., Nguyen, N.L., et al.: Temperature dependence of optical properties of MoS2 and WS2 heterostructures assessed by spectroscopic ellipsometry. Nanomaterials **15**, 76 (2025). https://doi.org/10.3390/nano15010076

Novoselov K.S., Mishchenko, A., Carvalho, A., Castro Neto, A.H.: 2D materials and van der Waals heterostructures. Sci. (1979). **353** (2016). https://doi.org/10.1126/science.aac9439

Oh, Y., Song, S., Bae, J.: A review of bandgap engineering and prediction in 2D material heterostructures: a DFT perspective. Int. J. Mol. Sci. **25**, 13104 (2024). https://doi.org/10.3390/ijms252313104

Pack, J.D., Monkhorst, H.J.: Special points for Brillouin-zone integrations"—a reply. Phys. Rev. B **16**, 1748 (1977). https://doi.org/10.1103/PhysRevB.16.1748

Pan, J., Zhang, Y.-F., Zhang, Y.-Y., Du, S.: Engineering two-dimensional magnetic heterostructures: a theoretical perspective. Nano Lett. **24**, 14909–23 (2024). https://doi.org/10.1021/acs.nanolett.4c04251

Pan, J., Wang, R., Zhou, X., Zhong, J., Xu, X., Hu, J.: Transition-metal doping induces the transition of electronic and magnetic properties in armchair MoS2 nanoribbons. Phys. Chem. **19**, 24594–604 (2017). https://doi.org/10.1039/C7CP03151C

Perdew, J.P., Burke, K., Ernzerhof, M.: Generalized gradient approximation made simple. Phys. Rev. Lett. **77**, 3865 (1996). https://doi.org/10.1103/PhysRevLett.77.3865

Pham, K.D., Phuc, H.V., Hieu, N.N., Hoi, B.D., Nguyen, C.V.: Electronic properties of GaSe/MoS2 and GaS/MoSe2 heterojunctions from first principles calculations. AIP Advances (2018). https://doi.org/10.1063/1.5033348

Rawat, A., Ahammed, R., Dimple, Jena, N., Mohanta, M.K., De Sarkar, A.: Solar Energy Harvesting in Type II van der Waals heterostructures of semiconducting group III monochalcogenide monolayers. J. Phys. Chem. C **123**, 12666–12675 (2019). https://doi.org/10.1021/acs.jpcc.9b03359

Singh, N.B., Mondal, R., Deb, J., Paul, D., Sarkar, U.: Density functional theory studies of van der Waals heterostructures comprised of $MoSi_2P_4$ and BAs monolayers for solar cell applications. ACS Appl. Nano Mater. **7**, 6704–6711 (2024). https://doi.org/10.1021/acsanm.4c00884

Talib, Z.A., Muhsen Almayyali, A.O., Rahman Jappor, H.: Strain-engineered 2D SiTe/AlSe heterostructure with high carrier mobility for enhanced optoelectronic and hydrogen evolution performance. Appl. Surf. Sci. **716**, 164653 (2026). https://doi.org/10.1016/j.apsusc.2025.164653

Togo, A.: First-principles phonon calculations with phonopy and phono3py. J. Phys. Soc. Japan (2023). https://doi.org/10.7566/JPSJ.92.012001

Tseng, C.-C., Song, T., Jiang, Q., Lin, Z., Wang, C., Suh, J., et al.: Gate-tunable proximity effects in graphene on layered magnetic insulators. Nano Lett. **22**, 8495–501 (2022). https://doi.org/10.1021/acs.nanolett.2c02931

Wang, V., Tang, G., Liu, Y.C., Wang, R.T., Mizuseki, H., Kawazoe, Y., et al.: High-Throughput Computational Screening of Two-Dimensional Semiconductors. J. Phys. Chem. Lett. **13**, 11581–11594 (2022). https://doi.org/10.1021/ACS.JPCLETT.2C02972/. (**SUPPL_FILE/JZ2C02972_SI_002.PDF**)

Witman, M.D., Jones, R.E., Rowberg, A.J., Adnan, S., Jin, M., et al.: Implementation strategies in phonopy and phono3py. J. Phys.: Conden. Matter **35**(35), 353001 (2023). https://doi.org/10.1088/1361-648X/ACD831

Wu, Y., Tong, J., Deng, L., Luo, F., Tian, F., Qin, G., et al.: Realizing spontaneous valley polarization and topological phase transitions in monolayer ScX2 (X = Cl, Br, I). Acta Mater. **246**, 118731 (2023). https://doi.org/10.1016/j.actamat.2023.118731

Xiao, Z., Li, Y., Yan, S., Bai, R., Zhou, T., Qiao, W.: GaSe/BiSCl Van Der Waals heterostructure for high-efficiency photocatalysis. J. Electron. Mater. **55**, 1939–1951 (2026). https://doi.org/10.1007/s11664-025-12635-7

Yang, F., Record, M.-C., Boulet, P.: Janus Ga2SSe-Based van der Waals heterojunctions as a class of promising candidates for photocatalytic water splitting: a dft investigation. Cryst. (Basel) **15**, 728 (2025). https://doi.org/10.3390/cryst15080728

Zhang, B., Lu, P., Tabrizian, R., Feng, P.X.L., Wu, Y.: 2D Magnetic heterostructures: spintronics and quantum future. Npj Spintronics. **2**, 6 (2024). https://doi.org/10.1038/s44306-024-00011-w

**Publisher's note** Springer Nature remains neutral with regard to jurisdictional claims in published maps and institutional affiliations.